Civil and Environmental Engineering
Publications

Civil and Environmental Engineering
Department

1-1-2023

Assessment of Tornado Alerting Performance for Canada

David M.L. Sills
Western University, David.Sills@uwo.ca

Lesley Elliott
Western University

Assessment of wind speeds along the damage path of the Alonsa, Manitoba EF4 tornado on 3 August 2018

Sarah A. Stevenson [a], Connell S. Miller [a], David M.L. Sills [a], Gregory A. Kopp [a,*],
Daniel M. Rhee [b], Franklin T. Lombardo [b]

[a] Northern Tornadoes Project, Faculty of Engineering, Western University, London, ON, Canada
[b] Department of Civil and Environmental Engineering, University of Illinois Urbana-Champaign, Urbana, IL, USA

ARTICLE INFO

ABSTRACT

Given the impracticality of attempting to directly measure wind speeds in tornadoes, wind speed estimation typically relies on the assessment of damage to structures and vegetation using classifications described in the Enhanced Fujita (EF) Scale. The advent of technology enabling the collection of large amounts of data, including detailed ground, drone, and aerial imagery, has led to a growth in research on non-conventional approaches for estimating tornado wind speeds. Research methods focused on defining the tornadic wind field based on forensic analysis of damage observations have shown promise for improving tornado assessments in a quantitative manner. In this study, novel methods for collecting forensic data following tornadoes are presented. Data from the Alonsa, MB tornado are applied to estimating the wind field along the damage path using treefall pattern analysis and threshold debris flight speed calculations. Comparison of the resulting wind speed estimates show reasonable agreement, with maximum speeds from both methods in the EF5 range. These research methods yield higher wind speeds than the maximum value obtained from the conventional EF-Scale assessment, which is in the low-end of the EF4 range based on a wood-frame house with sub-standard construction that was swept entirely from its foundation. Further work is still needed to make these methods operational for routine tornado intensity estimates.

1. Introduction

1.1. Background

Direct measurement of wind speed during a tornado is often impossible due to the unpredictable and violent nature of these storms. For this reason, tornado wind speeds are typically estimated and classified according to the levels and types of damage they inflict upon buildings and vegetation. Fujita (1971) proposed the first standardized method for classifying tornadoes. The Fujita Scale was used widely for over 30 years before it received significant updates to improve the accuracy of wind speed estimations and provide a more comprehensive list of structure types that can be used in tornado assessments (McDonald et al., 2009; Mehta, 2013). In 2006, researchers from Texas Tech University brought together a forum of Fujita Scale users to review and revise the scale, leading to the Enhanced Fujita (EF) Scale (Wind Science and Engineering Centre, 2006). In 2013, Environment Canada (2013)

further modified the EF Scale to better suit the Canadian context (Sills et al., 2014). The present study refers to the Canadian version of the EF Scale for assessment of residential structures and vegetation.

The Canadian EF Scale provides wind speed estimates for 31 Damage Indicators (DIs), which represent various structures or vegetation. For each DI, there are Degrees of Damage (DOD) that describe the sequential modes of damage that have been observed to occur. Each DOD has an associated upper-bound (UB), lower-bound (LB), and expected (EXP) wind speed. All DIs are assessed by observation of their final condition after the event. The predominant failure mode is determined and related to a DOD category, from which the estimated wind speed causing the damage is assessed. The EXP value is used unless documented features of the structure indicate that it was either of higher- or lower-than-normal construction quality or strength; in these cases, the estimated wind speed may be adjusted towards the UB or LB wind speed, respectively. The maximum estimated wind speed is then referenced to the EF-Scale wind speed ranges to categorize the intensity, from EF0 to EF5

(Mehta, 2013).

In assessing the damage path and intensity of a tornado, each individual building is assessed and given a rating. All building DIs assume that a rating will be assigned to each individual building. Similarly, the tree DIs in the original EF Scale (Wind Science and Engineering Centre, 2006) allows assessment of damage to individual trees, with one DI for hardwood trees and another for softwood trees. Subsequent research following the development of the original EF Scale found that the difference between hardwood and softwood tree damage was less than previously thought, and not as important as other factors (Frelich and Ostuno, 2012). As a result, the Canadian EF Scale was developed with a single tree DI (C-T) using a population-based approach that had been used historically in Canada with the Fujita scale (Sills et al., 2014). Examples for two of the most common DIs in Canada (Sills et al., 2020) – Residential Structures (FR12) and Trees (C-T) – are provided in Tables 1 and 2, respectively.

Remote sensing technologies, such as satellites and unmanned aerial vehicles (UAVs, commonly referred to as drones) are becoming more widely used and enable new possibilities for the assessment of tornadoes (Womble et al., 2007; Radhika et al., 2012; Radhika et al., 2015; Womble et al., 2017; Womble et al., 2018). One approach involves the use of treefall patterns to estimate the wind field along the damage path as well as the maximum wind speed. The calculation of threshold wind speeds for the lofting of large wind-borne debris can also be used as an independent estimate of tornado intensity, with the locations of the debris estimated using remote sensing. The objective of this study is to apply these two methods for wind speed estimation to the EF4 tornado that hit Alonsa, Manitoba, Canada on August 3, 2018, compare their results to that from the conventional EF-Scale assessment of that event, and evaluate the degree to which the research methods increase wind speed consistency and accuracy.

This paper introduces the ground, aerial, and satellite survey methodology applied to capturing data following the Alonsa tornado and compares several approaches to assess tornado wind speeds based on the damage observations. A conventional EF-Scale assessment is carried out based on ground observations of structural damage as well as estimates of treefall quantity based on inspection of aerial imagery. Two novel methods for wind speed estimation are then presented, and wind speed estimates are compared to those from the conventional method. First, a

Table 1
DOD descriptions and wind speed estimates for the FR12 DI, as adopted by Environment and Climate Change Canada (2013).

DOD	Description of Damage	Wind Speed Estimates [km/h]		
		Lower Bound	Expected	Upper Bound
1	Threshold of visible damage	85	105	130
2	Loss of roof covering material (up to 20%), gutters and/or awning; loss of vinyl or metal siding	100	125	155
3	Broken glass in door and windows	125	155	185
4	Uplift of roof deck and loss of significant roof covering material (more than 20%); collapse of chimney; garage doors collapse inward; failure of porch or carport	130	155	185
5	Entire house shifts off foundation	165	195	225
6	Large sections of roof structure removed (more than 50%); most walls remain standing	165	195	230
7	Exterior walls collapsed	180	210	245
8	Most walls collapsed, except small interior rooms	205	245	285
9	All walls collapsed	230	275	320
10	Destruction of engineered and/or well-constructed residence; slab swept clean	265	320	355

Table 2
DOD descriptions and wind speed estimates for the C-T DI, as adopted by Environment and Climate Change Canada (2013).

DOD	Description of Damage	Wind Speed Estimates [km/h]		
		Lower Bound	Expected	Upper Bound
1	Small limbs broken (less than 2 cm diameter)	55	70	85
2	Large branches broken (2–8 cm diameter)	65	90	110
3	Up to 20% of mature trees snapped and/or uprooted	80	115	150
4	More than 20% of mature trees snapped and/or uprooted	105	150	190
5	More than 50% of mature trees snapped and/or uprooted	145	190	230
6	More than 80% of mature trees snapped and/or uprooted; numerous trees may be denuded/debarked by missiles with only stubs of largest branches remaining	190	235	275

calculation method is developed for estimating wind speeds required to loft large debris items. The second method uses patterns in treefall observed form aerial imagery to estimate parameters of the tornado wind field. The study concludes with a discussion and comparison of the research methods.

1.2. Methods for tornado wind speed assessment

There has been a significant amount of research to estimate wind speeds in tornadoes. One of the most common approaches has been to assess the expected performance of buildings and their structural components using fragility functions. Fragility curves have traditionally been developed analytically (Rosowsky and Ellingwood, 2002; Ellingwood et al., 2004; Lee and Rosowsky, 2005; Amini and van de Lindt, 2014) to provide the probability of a component exceeding a certain limit state under a range of loading conditions. Such functions have been developed and applied to estimating failure wind speeds in straight-line winds and tornadoes, as well as predicting the performance of mitigative measures. The use of fragility functions for residential structures has also been useful for refining EF-Scale wind speed estimates in tornadoes and, thus, improve the understanding of the near-surface wind fields (Roueche and Prevatt, 2013; Amini and van de Lindt, 2014; Morrison et al., 2014; Kopp et al., 2016; Roueche et al., 2017). While the FR12 DI has been extensively studied, there is a need for similar development of other DIs (Edwards et al., 2013) as well as the use of other approaches.

One method of improved wind speed estimation for tornadoes exists in assessment of treefall patterns, given the prevalence of tree damage in tornadoes. Although the tree DIs with both the US and Canadian implementations of the EF Scale allow rapid estimation, assessment is limited in nearly all cases to a maximum rating of EF3. Several research-oriented methodologies for more accurately assessing tornado intensity (including EF4-5) based on treefall have been developed in recent years, inspired by the pioneering work of Johannes Letzmann (Peterson, 1992). Historically, ground surveys of damage to forested areas have been used to provide qualitative information related to patterns in treefall direction, where the nature of the storm can be inferred from the direction of treefall (Rhee et al., 2021). Other qualitative assessments may look at debris fields and breakage of the trunk versus uprooting of the whole tree (Gardiner et al., 2000; Godfrey and Peterson, 2017). Bech et al. (2009) and Beck and Dotzek (2010) made a qualitative assessment of tornado intensity in forests by comparing the treefall directions observed from ground surveys to theoretical treefall damage patterns by simulating a tornado with a Rankine vortex model.

Recently, more rigorous methods of quantitatively comparing

treefall patterns and reconstructing the tornado wind field were developed (Karstens et al., 2013; Lombardo et al., 2015; Rhee and Lombardo, 2018). Based on the previous works, Chen and Lombardo (2019) developed an analytical solution that can provide the Rankine vortex parameters without having to numerically simulate a tornado. With statistical sampling from observed trees coupled with a wind-and-tree resistance model, Godfrey and Peterson (2017) constructed a distribution of treefall percentage in forested areas and used the proportion of damaged trees to assess the intensity of the tornado, similar to the Canadian C-T DI. These various methods of assessing the tornado intensity based on tree damage are commonly referred to as treefall analysis. In Lombardo et al. (2015), treefall analysis was used to estimate near-surface winds of the May 2011 Joplin, Missouri EF5 tornado. A comparison of the treefall wind field to wind speeds estimated according to the EF scale (US version) for nearby structures showed that the treefall estimates were consistently higher than the EF-Scale assessment, with larger differences in lower wind speed regions. The present study extends this work by applying a similar treefall model to a heavily forested area rather than a suburban setting where trees are more scattered.

One common feature of a strong tornado is wind-generated debris, caused by wind speeds exceeding the threshold for lofting various elements into the air. Wind-borne debris can be a major cause of additional damage. In addition to the damage caused by debris impacts on buildings and vehicles, the movement and flight of various items including farm equipment, hay bales, and other building contents result in additional losses. The movement of such items can provide further insight into tornado wind speeds. However, there are several challenges with estimating wind speeds from field observations of debris. Wind speeds are significantly affected by the presence of structures and other obstacles. For example, the failure and subsequent flight of small projectiles such as roof sheathing depend intimately on the local flow field above the roof and the wake downstream of the structure, as well as the gust duration and the geometry and mass of the debris element (Kordi and Kopp, 2011). For larger elements, like a complete roof, this is also true (Kopp et al., 2011); however, the modification of the flow field is likely to be less important while the gust duration may play a larger role due to the relatively slow accelerations of larger, heavier objects. The second challenge is that wind velocity changes continuously during a tornado event; typically starting with lower velocities, increasing to a maximum, and then decreasing. In addition, there is turbulence making peak gust wind speeds difficult to determine. Finally, tornadic events also have a significant vertical wind component, which can loft heavy objects. (McCarthy et al., 2008; Haan et al., 2017). Based on when the actual failure or lofting of the object occurs, how long the projectile takes to accelerate, and the horizontal velocity required to keep the object aloft, the wind velocity initiating failure is different from the velocity required to sustain flight of the object. Due to the complexity of the wind field and debris behaviour, simplifying assumptions are required to estimate the threshold wind velocity causing flight of certain debris items based on field observation. Some estimates are made in the current paper to augment the wind speeds estimated from treefall and damage to buildings.

2. Alonsa, MB tornado details and post-storm survey

On the evening of August 3, 2018, a violent tornado developed in south-central Manitoba. Two injuries and one fatality resulted at locations where severe structural damage was observed. Based on ground surveys conducted in the days following the event in collaboration with Northern Tornadoes Project (NTP), Environment and Climate Change Canada (ECCC) assessed the tornado's maximum wind speed to be 275 km/h, rating its intensity as a low-end EF4 on the Enhanced Fujita Scale (Environment Canada, 2013). This was the first tornado in Canada to be rated EF4 under the Enhanced Fujita Scale and the highest-rated Canadian event since the F5 Elie, Manitoba tornado that occurred in 2007, about 130 km SE of Alonsa.

The tornado resulted in a damage path 15.7 km in length and with a maximum width of 1600 m. Fig. 1 shows an overview of the damage track with ground survey sites labelled for reference in the following discussion. Sites numbered 1 through 7 have been labelled on the map to indicate areas of structural damage noted on the ground survey. In between these areas, the majority of the damage was to low-lying vegetation and trees. It is estimated that roughly $2 M in damage resulted from the tornado, mostly to the small farm buildings, single-family homes, recreational trailers, farm equipment and vehicles (Sills et al., 2020).

2.1. Overview of tornado development and meteorological prediction

In the days leading up to August 3, 2018, a synoptic-scale pattern favourable for severe convective storms brought active weather to Alberta and Saskatchewan with large hail reported in both provinces. This same pattern resulted in the occurrence of severe weather in southern MB on August 3. As an upper-level ridge pushed eastward into northwestern ON, an upper-level jet moved over southern MB. An associated surface low continued to track east from southern SK and by 7:00 p.m. local time (LT, CDT) an occluded front extended south from the surface low to the US border, with Alonsa just east of the boundary.

With warm, moist southerly flow at the surface ahead of the front, the mixed-layer Convective Available Potential Energy at 7:00 p.m. LT reached a level considered high (up to 4000 J kg^{-1}) in the Parkland region where there was little to no mixed-layer Convective Inhibition. The wind regime in place at that time, with Effective Bulk Shear up to 40 kt, supported the development of supercell thunderstorms (i.e., storms having a persistent, rotating updraft) and a heightened risk of a significant (EF2+) tornado. In fact, the unitless Supercell Composite Parameter reached as high as 20 at 7:00 p.m., indicating a high risk of supercells. Another useful index, the unitless Significant Tornado Parameter, reached over 3 at that time, indicating an elevated threat of a significant tornado. The environmental parameters presented here are derived from the hourly mesoanalysis product from the NOAA Storm Prediction Center's website (National Oceanic and Atmospheric Administration, 2020).

A discrete thunderstorm rapidly developed in south-central Manitoba, with clearly identifiable supercell features once the storm was within the range of the Woodlands weather radar by 8:20 p.m. LT. A velocity couplet associated with a mesocyclone (with data dropouts where a tornado would be expected) along with a strong reflectivity core and hook echo were present for several scans, including at 8:40 p.m. LT as shown in Fig. 2. The approximate location of the mesocyclone detected by radar at 8:20 p.m. is in the vicinity of the start of the tornado damage path identified by the post-event ground surveys south of Alonsa. Hence, the tornado start time is estimated to be 8:20 p.m. Eyewitness video captured the powerful tornado near Alonsa at around 8:30 p.m. LT (shown in Fig. 3, taken facing north). The tornado tracked northeast for 15.7 km to Lake Manitoba, and it is unknown at what point the tornado dissipated over the water. The supercell was overtaken by a line of thunderstorms as it reached the Lake's eastern shore. The tornado was over land for at least 25 min and the parent supercell traveled approximately 50 km over the course of an hour.

2.2. Damage survey and aerial data collection

NTP team members collaborated with ECCC staff on ground surveys, initially on the day after the tornado (August 5) and then again on August 8 and 9. The EF4 rating was based mainly on the results of these surveys, much of which is presented here. The ground surveys and analysis of high-resolution satellite imagery provided a preliminary damage track, which was used to define the flight plan for an aircraft aerial survey that was conducted on August 10. The aerial photography provides high-resolution (5 cm) imagery and covers the majority of the track except for a portion surrounding the start of the damage path.

Fig. 1. Overview of Alonsa tornado path as viewed with satellite imagery, with ground survey sites with EF-Scale assessments of structural damage labelled.
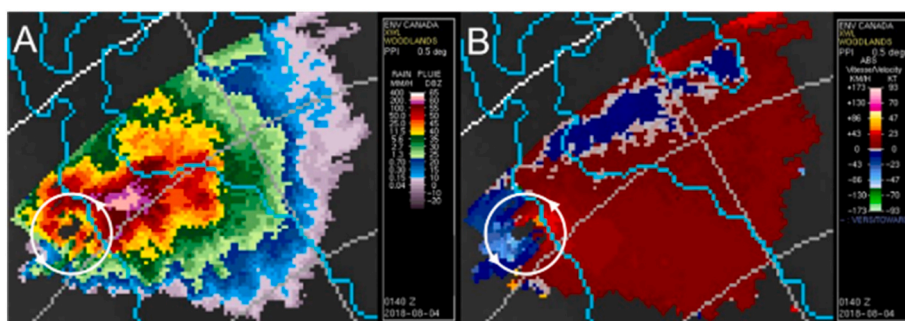

Fig. 2. XWL C-band Doppler weather radar products depicting (A) reflectivity and (B) radial velocity in the Alonsa, MB area at 0140 UTC (8:40 p.m. LT) on August 3, 2018. The area of rotation detected in the radial velocity for this supercell is circled in white and also superimposed on the storm reflectivity.

Early review of satellite imagery did not reveal the start of the path due to poor visibility, so the start of the path was not identified until after the aerial survey was flown. The full survey dataset is available on the NTP 'open data' website for public access and use in further research (Northern Tornadoes Project, 2020).

The ground-based damage surveys conducted by the NTP team covered the sites shown in Fig. 1, with drone surveys used to capture detailed aerial footage of each site, and to fill in sections of the path between residential sites. Drones were also used to capture additional details related to vegetation damage and to provide an additional point of comparison between the ground, aerial, and satellite observations. Significant structural damage was observed at Sites 2 through 7, with the EF4-rated damage (FR12, DOD9) occurring at Site 3. The various survey results are discussed further below.

2.2.1. Ground survey and EF-scale assessment of damage to structures

A residential structure with DOD9 (FR12, Lower Bound Wind Speed 230 km/h or EF2) damage was observed at Site 2. Local residents reported that the house at this property had been abandoned prior to the storm, and that some windows may have been missing. The house appeared to be of older construction. The roof and most exterior walls were removed from atop basement walls, as shown in Fig. 4. Upon closer inspection, the sheathing material and wall baseplates appeared to be rotten. This structure was rated as DOD9 because all walls had effectively collapsed, other than short wooden knee walls on top of the basement concrete walls. Drone surveys located a refrigerator, believed to have come from the house or an outbuilding on the same property, about 80 m to the east.

The tornado appeared to reach its greatest intensity in the region nearing Site 3. A house and several farm outbuildings were completely swept away, and there was evidence of vehicles and farm equipment being lofted significant distances. Large trees close to the house were ripped out of the ground, including much of the root structure, and thrown more than 10 m. A chest freezer originating in the house, was found 200 m away. The house at Site 3 was swept from the foundation, as shown in Fig. 5. The original house was constructed in the 1950's and appeared to be firmly anchored to the foundation. However, two additions were observed to have poor connections between the walls and the foundation. Due to the direction of travel of the tornado and orientation of the structure, it is expected that the failure of this house may have initiated in the southern addition, where the walls were removed from atop the plywood subfloor. Cascading failure of the remaining structure is assumed to have occurred. Some of the wooden baseplates of the original structure were still in place with appropriate anchor bolts. Considering that the entire house was not considered to be "well-constructed", DOD10 for FR12 was deemed inapplicable and the structure was assessed at DOD9 (FR12 – EXP wind speed 275 km/h or EF4). A number of barns and outbuildings on the property were also swept away completely. DOD8 is the highest degree of damage applicable to the SBO DI, described as "total destruction of building." Given the buildings were swept away, SBO DOD8 UB was assigned giving a wind speed of 210 km/h. It is noted that the wind speed estimates associated with some DIs, such as SBO, are of limited use for assessing strong events because some structure types are only strong enough to resist a relatively low level of wind loading.

The residential property at Site 4 was located in close proximity to Site 3, but at the northern edge of the damage path; observed damage was less severe than at neighboring properties. The house on this property had some shingles removed and the vinyl siding had minor damage (FR12, DOD3 – EXP wind speed 155 km/h or EF1). A shed structure in the same yard was removed from its foundation slab (SBO, DOD8 – EXP wind speed 180 km/h or EF2). The anchor bolts were intact but bent, and the entire wood (metal-clad) structure was removed. The contents of the shed remained mostly intact.

At Site 5, a house built in 1993 lost its roof and three exterior walls (FR12, DOD8 - EXP wind speed 245 km/h or EF3). Inspection of a portion of the roof found on the property indicated that the roof-to-wall connections were toe-nailed, and the roof was of stick-frame

Fig. 3. Screen capture from video by Shawn Cabak showing the Alonsa, MB, tornado at its most intense. Used with permission.

construction. The homeowners, who hid beneath a dining table during the storm, reported that they saw the roof lift off from above them before the walls collapsed. The failed exterior walls enclosed a large open living space, while closely spaced walls enclosing small rooms remained standing. One potential weakness in the failed exterior walls was the nailed connection from the bottom plate of the wall, through the plywood subfloor into the floor framing. This detail is shown in the inlay of Fig. 6. On the same property, several farm structures and a log cabin outbuilding were removed from their foundations (SBO, DOD8 – EXP wind speed 180 km/h or EF2) but were not observed to have been well-anchored.

The Site 6 property was the last residential property and farmstead impacted by the tornado before it reached and eventually dissipated over Lake Manitoba. This property includes a residential yard on the north side of the road, and farm structures and cattle fences across the road to the south. The homestead included a newer residential structure with no visible damage. Further north along the driveway a cottage in the same yard was completely removed from its foundation (FR12, DOD9 – Lower Bound Wind Speed 230 km/h or EF3). Based on its usage

and size, the FR12 DI was chosen because it was the most fitting DI available, but the LB wind speed was assumed due to the lack of anchorage. Fig. 7 shows the remaining basement and collapsed concrete block basement walls. Discussions with the resident revealed that the cottage was built in 1963, but the basement was constructed later and the building was then lifted and moved atop the basement walls. There were no fasteners between the wood structure and the top of the concrete block walls. Debarked trees were also noted at this property.

Significant debris was found washed up on the shore at Site 7, as discussed in Section 4.1. Several vehicles and trailers were found in the lake, some having been moved prior to the damage survey. Numerous camping trailers suffered severe damage or were overturned in the campground, in addition to several cottages that were destroyed. One log cabin cottage was pushed off its piers, but otherwise suffered minor exterior damage. Site 7 was not assessed for an EF-Scale rating due to the lack of damage indicators for vehicles and these types of structures.

Finally, an EF-Scale assessment of damage to trees was made at several locations, making use of aerial imagery. The population of trees down was estimated by visual inspection within an approximately square area as wide as the extent of damage on each property using the 'forest box method' (Sills et al., 2020). While there is no DOD in the Canadian tree DI for removal of entire trees from the ground (as observed at Site 3), DOD6 does make reference to tree debarking which was observed at Site 6. Therefore, the DOD6 EXP wind speed is assumed at that location. Table 3 provides a summary of the DIs, rated DOD categories, and wind speed estimates based on the ground survey observations for structural DIs and aerial imagery for the C-T DI.

2.2.2. Satellite review

Guided by the storm track identified with XWL radar products, a review of high-resolution satellite imagery was conducted. NTP specifically uses a quasi-daily satellite service known as Planet Labs. Their Planetscope satellites capture the visible spectrum in red, green, and blue (RGB) bands, as well as a near infrared (NI) band at a nominal resolution of 3 m. These images are automatically orthorectified, radiometrically corrected, as well as corrected at the top and bottom of the atmosphere to reduce spectral inconsistency across time and location. Clear satellite imagery (i.e., cloudless, smoke free, and haze free) from prior to the event, as well as from directly after the event were obtained from dates as close as possible to the day of the tornado. This analysis covered approximately 1300 km^2 in the Rural Municipality of Alonsa (west of Lake Manitoba) and R. M. of Eriksdale (east of Lake Manitoba), where land-use is a mix of aspen parkland, boreal forest, and agriculture. An outline of visible damage is shown in Fig. 8. Tornado damage in the area surrounding the highway to the left side of Fig. 8 is clearly visible when comparing satellite imagery from mid-July to early September. A unique challenge in identifying damage with satellite imagery for this event was smoke and haze drifting across the Prairies into MB from forest fires in Alberta and British Columbia and reducing image sharpness. The smoke impacted the region for several weeks until late August, after which the clearer imagery revealed some weak tree damage at Site 0 and sporadic weak damage leading to Site 1.

An estimate of the maximum width along the path of 800 m was made by the ground survey team. Analysis of aircraft aerial imagery resulted in a significant increase of the maximum path width to 1200 m. However, it was noted that tree damage extended to the edges of this aerial imagery in several locations, suggesting a width greater than 1200 m. High-resolution satellite imagery was eventually used in combination with the aircraft aerial and ground survey damage locations to reach an estimate of 1600 m for the maximum width. The damaging wind field of the tornado widened beyond Site 2 and reached an observed maximum near Site 6.

2.2.3. NDVI analysis

Since the area of the tornado was a mix of trees and cropland, it was difficult to visually detect the full path. To help with visualization, a

Fig. 4. Damage to abandoned residential structure at Site 2, assessed as DOD9 of FR12. Inset shows closer view of remaining knee wall.

Fig. 5. Drone and ground photos of damage to house at Site 3, assessed as DOD9 of FR12. Red arrow indicates direction of travel of the tornado, and the yellow arrows indicate the direction of rotation.

Fig. 6. Drone image of DOD8 damage at Site 5. Inset shows edge of floor structure; exposed plywood indicates location where walls used to sit.

Normalized Difference Vegetation Index (NDVI) analysis was performed on the satellite imagery. NDVI is a measure of vegetation health based on how the plant reflects light at the near-infrared and red frequencies. In particular, NDVI is defined as:

Fig. 7. Drone image showing collapsed basement walls from cottage at Site 6. Inset shows location where floor joists from cottage sat atop of the concrete block basement walls.

Table 3
Listing of Canadian EF-Scale assessment at damage survey sites.

Site	Damage Indicator	Degree of Damage	Wind Speed Estimate [km/h]	EF-Scale Rating
0	C-T	4	150	1
1	C-T	6	235	3
2	FR12	9	230	3
3	FR12	9	275	4
3	SBO	8	210	2
3	C-T	6	235	3
4	FR12	3	155	1
4	SBO	8	180	2
5	FR12	8	245	3
5	SBO	8	180	2
6	FR12	9	230	3
6	SBO	4	145	1
6	C-T	6	235	3

$$NDVI = \frac{NIR - RED}{NIR + RED} \qquad (1)$$

where NIR is the reflection in the near-infrared spectrum, and RED is the reflection in the red spectrum. This index works well for vegetation because chlorophyll, which is a health indicator for vegetation, reflects near-infrared light and absorbs visible light. Therefore, if there is less chlorophyll, more near-infrared light is absorbed, and more visible light is reflected (compared to the healthier plant). Thus, observing an index consisting of the near-infrared and red spectrum is an appropriate way of measuring plant health. NDVI values always fall between -1 and 1, where negative values are created from areas such as clouds and water, values close to 0 are created from bare soil, and positive values are created from areas with plants, trees, or other vegetation. Therefore, this index can be used to detect when the tornado began to affect the crops below it, allowing determination of the path.

This NDVI index has been used empirically to measure the change in vegetation health caused by tornadic ground scour for single events in many previous studies (Womble et al., 2018). From May 2 to May 8, 1999, over 150 tornadoes impacted the Oklahoma region, with damage peaking in Bridge Creek-Moore with a tornado, which was rated F5. Magsig et al. (2000), and Yuan et al. (2002) used NDVI analysis from the Indian Remote Sensing satellite to assist with the detection of tornado tracks from that outbreak, while Myint et al. (2008) compared image processing techniques from this outbreak using Landsat imagery.

To account for the starting plant health of the crops in the Alonsa event, a percent change equation was implemented by comparing the

before and after satellite imagery (Yuan et al., 2002), or:

$$NDVI_{\%Change} = \frac{NDVI_{After} - NDVI_{Before}}{NDVI_{Before}} \qquad (2)$$

Fig. 9 shows the NDVI visualization of the Alonsa tornado overlain on the satellite imagery of the path. Red values indicate a decrease in vegetation health, green values indicate an increase in vegetation health, whereas transparent values indicate no change to vegetation health. The intensity of this NDVI change is not expressed in the Figure due to complexities in changing crop types across the damaged area, as well as the fact that the NDVI is also picking up color changes from fallen trees in the area. Future work should be done to account for variation in land cover, and its effect on the intensity of change in NDVI values. Debris removal and events such as crop harvesting occurring after the event can alter the NDVI in ways that are unrelated to tornadic damage (Molthan et al., 2014). Typically, large fields that are completely labelled in red have had their vegetation health decreased due to harvesting activities, and fields that are completely labelled in green have had their vegetation health increased due to planting activities, or in the case of water and wetlands, due to algae bloom. In addition, regular seasonal changes in vegetation can also affect the NDVI difference depending on the length between useable satellite imagery (Kingfield and deBeurs, 2017); this can be seen in the southwestern portion of the image. Finally, the area between Site 0 and Site 1 shows little damage to vegetation.

3. Wind-borne debris analysis

3.1. Observations and data

Some of the significant debris items observed in this tornado were large vehicles, including tractors, farm equipment, trucks, RVs, and campers. Fig. 10 shows photographs from the ground survey showing displaced vehicles. The majority of these vehicles originated (recounted by the vehicle owners during the ground survey) from locations near the homes on the edge of Lake Manitoba to the northwest of Site 7. Ground survey observations (from homeowner recollection, as well as examining debris patterns in the sand) showed that the majority of these vehicles were lofted rather than rolled or tumbled to their end points. This was especially clear with passenger vehicles and trailers that landed in the lake; some were located by drone imagery, dozens of meters from the shore while others were found along the beach. Haan et al. (2017) performed wind tunnel and tornado simulator studies on model vehicles to determine their debris threshold wind speeds. The data from their
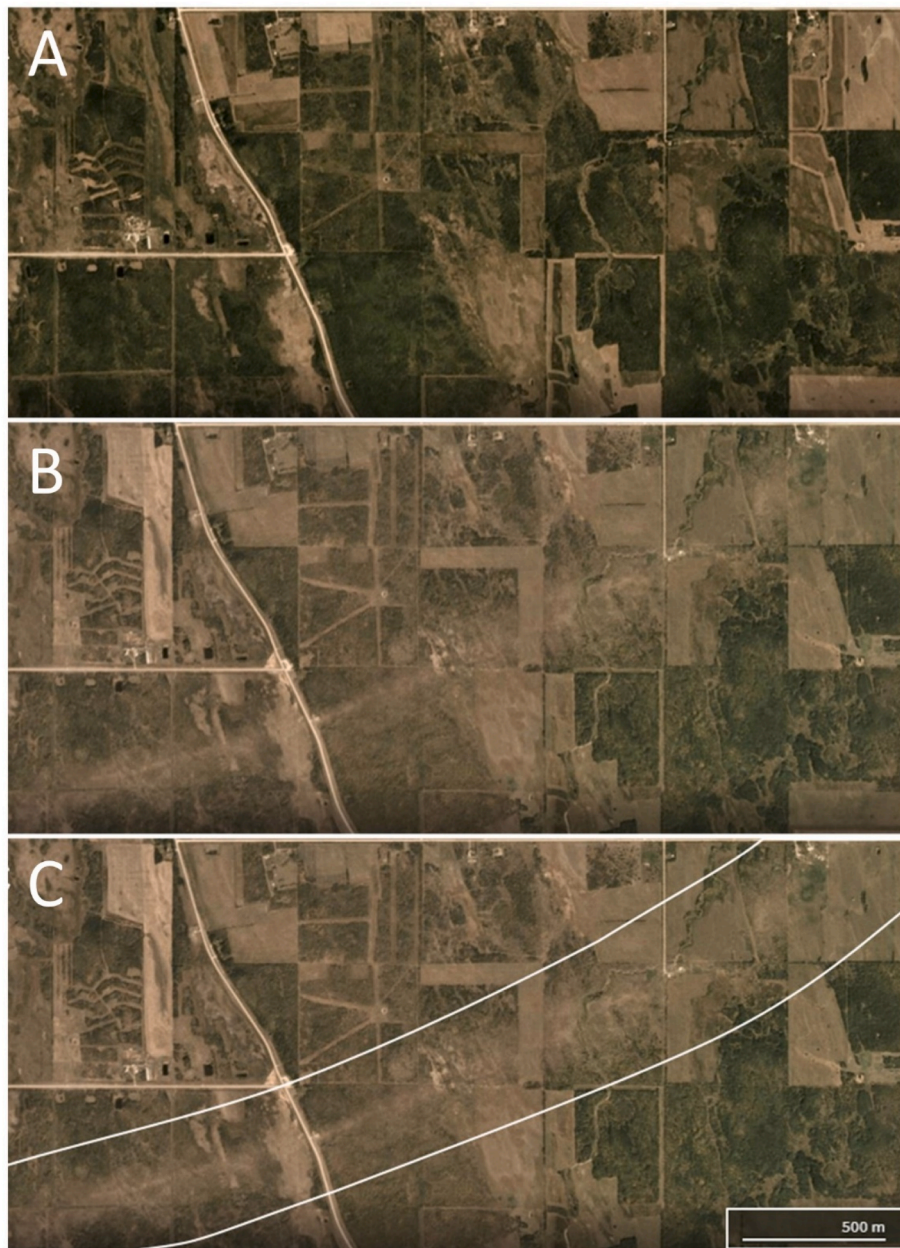
Fig. 8. Satellite imagery review of the Alonsa area showing difference in land cover appearance before and after the tornado. (A) was captured on July 17, 2018, and (B) & (C) are from September 3, 2018. (C) Shows the analyzed extent of the damage path with a white outline.
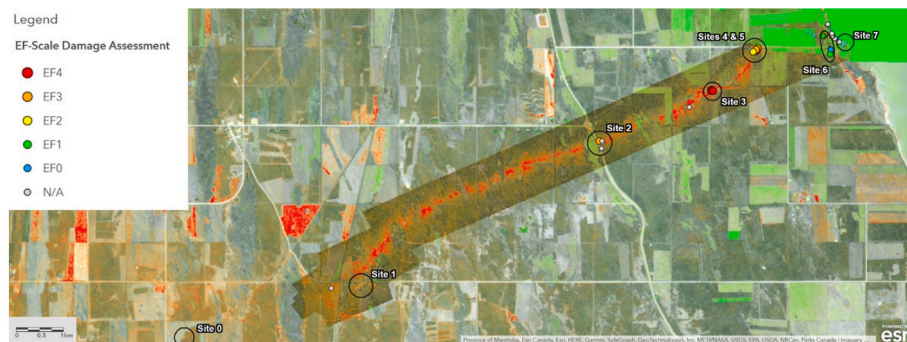

Fig. 9. Overview of the Alonsa tornado damage track including labelled ground survey sites. Satellite imagery of the path is overlaid with NDVI, which indicates the areas of damage to vegetation.

Fig. 10. Ground survey photos showing farm vehicles, passenger trucks, and camper trailers that were lofted by the tornado.

study predicts that the onset of lofting of vehicles tends to occur in the high-end EF3 to EF4 range.

Another common debris type observed in the damage survey was the cylindrical hay bale. Over 100 of these were removed from fields between Site 4/5 and Site 6, with some landing among the downed trees to the east and many others apparently landing in Lake Manitoba before being broken down and pushed back to the shore. Several partially intact hay bales were found washed up on the beach at Site 7 (see Fig. 11). Due to their uniform cylindrical shape and having uniform density, these hay bales are an ideal subject for debris flight analysis. Although it is impossible to determine their exact start points, Fig. 12 shows the locations of the fields from which they originated. The hay bales would have had to travel at least 500 m, and up to a maximum of 2000 m, to reach the Lake. Wills et al. (2002) states that loose-laid objects tend to roll or tumble along the ground rather than be lofted. However, there were few signs of hay debris in the fields and the hay bales would have to travel over wooded areas and structures to reach the Lake. Therefore, it appears that the hay bales were, in fact, lofted and a wind field with a strong vertical wind component is assumed to have been present.

3.2. Threshold flight analysis

In order to obtain an estimate of the potential wind speeds required to loft hay bales, the threshold wind speed for lofting can be obtained from the projectile motion equations. To start, the aerodynamic force acting on a compact object can be generally expressed as:

$$F = \frac{1}{2}\rho_a(U - U_m)^2 A C_D \tag{3}$$

where F is the aerodynamic force, ρ_a is the density of air, U is the wind speed, U_m is the speed of the object, A is the reference area of the object, and C_D is the drag coefficient. Applying Newton's 2nd law in both the horizontal and vertical direction, the instantaneous acceleration of a compact object is given by:

$$\frac{d^2x}{dt^2} = \frac{\rho_a}{2\rho_m l}(C_D \cos\Theta - C_L \sin\Theta)\left[(X - x_m)^2 + (Z - z_m)^2\right] \tag{4}$$

$$\frac{d^2z}{dt^2} = \frac{\rho_a}{2\rho_m l}(C_D \sin\Theta + C_L \cos\Theta)\left[(X - x_m)^2 + (Z - z_m)^2\right] - g \tag{5}$$
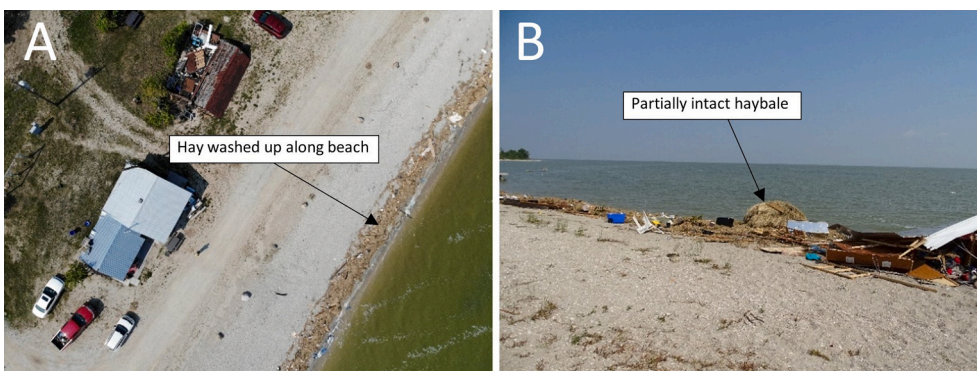

Fig. 11. Drone photograph and ground photograph of hay bale debris that were lofted into Lake Manitoba by the tornado.
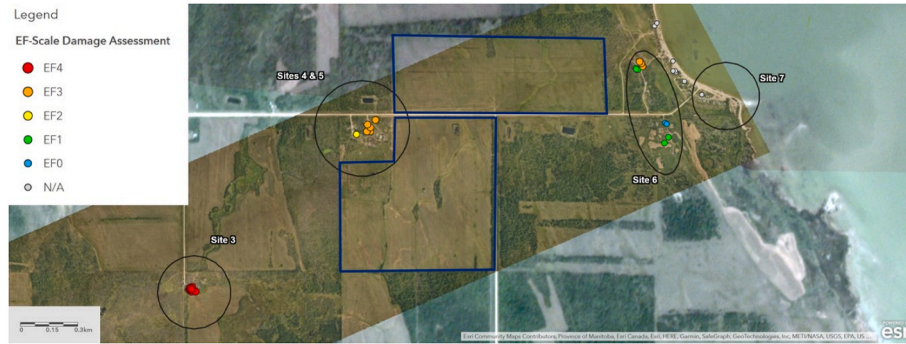
Fig. 12. Estimated originating locations of hay bales that were carried to the lake (right side of image). Fields outlined with blue contained bales prior to the tornado.

where $\frac{d^2x}{dt^2}$ and $\frac{d^2z}{dt^2}$ are the horizontal and vertical acceleration of a compact object, respectively, ρ_a is the density of air, ρ_m is the density of the debris (assumed uniform through the object), g is the gravitational constant, l is the characteristic dimension of the object, Θ is the angle between the resultant wind speed and the horizontal axis, C_L is the lift coefficient, X and Z are the horizontal and vertical wind speed, respectively, x_m and z_m are the horizontal and vertical speeds of the object, respectively. This model for the acceleration of debris in a wind field has been commonly used in trajectory analysis in previous studies (Holmes, 2004; Baker, 2007; Baker and Sterling, 2017; Huo et al., 2020; Zhao et al., 2021). This derivation assumes that there is no rotation of the compact object while in the air, and therefore, there are no additional lift forces due to the Magnus effect (Holmes, 2004).

If the projectile does not move before it is lofted ($\frac{d^2x}{dt^2} = 0, x_m = 0, z_m = 0$), the equation for the acceleration in the vertical direction can be expressed as:

$$\frac{d^2z}{dt^2} = \frac{\rho_a}{2\rho_m l}(C_D \sin \Theta + C_L \cos \Theta)[X^2 + Z^2] - g \quad (6)$$

To solve for the threshold lofting wind speed of an object, the vertical acceleration ($\frac{d^2z}{dt^2}$) is set to equal zero, as the projectile will take flight when $\frac{d^2z}{dt^2} > 0$. Rearranging for the threshold lofting speed yields,

$$v_{Threshold} = \sqrt{X^2 + Z^2} = \sqrt{\frac{2g\rho_m l}{\rho_a[C_D \sin \Theta + C_L \cos \Theta]}} \quad (7)$$

This model requires an estimation of the drag and lift coefficient for objects of irregular sizes (which are often obtained via wind tunnel testing). To simplify this, a similar method to that in Chai et al. (2019) can be used. The shape of the object was estimated to be somewhere between two extreme shapes, an ellipsoid (sphere) and a cuboid (cube). A shape factor can be defined as a ratio of the change in volume between the debris and the cuboid over the change in volume between the ellipsoid and the cuboid, or,

$$S_p = \frac{V_{Debris} - V_{Cuboid}}{V_{Ellipsoid} - V_{Cuboid}} \quad (8)$$

If the debris object is a perfect sphere, the shape factor is equal to 1, and if the debris object is a perfect cube, the shape factor is equal to zero. Using this, the drag coefficient can be defined as:

$$C_{D,Debris} = (S_p)C_{D,sphere} + (1 - S_p)C_{D,cube} \quad (9)$$

Similarly, the equation for a lift coefficient for debris can be defined as:

$$C_{L,Debris} = (S_p)C_{L,sphere} + (1 - S_p)C_{L,cube} \quad (10)$$

The lift and drag coefficients of a stationary surface-mounted sphere, and a stationary surface-mounted cube introduce uncertainty into this equation, which are dependent on the Reynolds number and the angle of

attack. Therefore, a range of values are presented in order to determine the range of threshold wind speeds. From studies by Jesson et al. (2015), and Haines and Taylor (2018), the lift coefficient of a stationary surface-mounted cube is noted to be in the range of 0.4–0.55 while the drag coefficient is about 1.0–1.1. From the study by Tsutsui (2008), the lift coefficient of a stationary surface-mounted sphere is in the range of 0.27–0.35 while the drag coefficient is within about 0.35–0.49.

Another source of variation is the vertical component of wind (expressed in Eq. (7) as Θ). The Twisdale et al. (1981) tornado wind field model (which was originally developed for wind-borne debris analyses) shows that the vertical component of wind in a tornadic wind field can range from $0°$ up to a maximum of about $15°$ at an elevation of 1 m for a translating tornado. Therefore, this range of values is used in the calculation to demonstrate the uncertainty this creates in the threshold wind speed estimation.

To assess the validity of this simple model, it can be applied and compared to the minivan tested in Haan et al. (2017) in a tornado-vortex simulator. These authors conducted model-scale studies of a minivan in both a straight-line wind tunnel, to determine the onset wind speeds for sliding, as well as a tornado vortex generator, to determine the onset wind speeds for sliding, flipping, and lofting. During their tornado-vortex testing, the motion of the vehicle was restricted to ensure that flipping and lofting occur before sliding. Table 4 presents the assumptions made in the calculation of the threshold lofting flight wind speed for the minivan using the above equations, along with Haan et al.'s (2017) results for the 3-s peak gust speed required to loft the same vehicle type at different model scales and subjected to different vortices. The drag coefficient was taken directly from the value used in Haan et al. (2017), although no lift coefficient was provided. The instantaneous $X_{Threshold}$ values calculated in the present analysis are converted to $\hat{U}$, 3-s gust speeds, using the method in Durst (1960) for direct comparison to the results presented in Haan et al. (2017).

This threshold flight model gives comparable results to the that presented in Haan et al. (2017), noting that there is considerable uncertainty in the aerodynamic coefficients, the angle of attack and the correction to the 3-sec gust. Of note, the $15°$ vertical angle of attack has the effect of reducing the threshold wind speed by about 10% over purely horizontal winds. Though several vehicles were lofted by the Alonsa tornado, pickup trucks and tractors are different enough aerodynamically from minivans that flight analyses are not attempted here.

Table 5 presents the assumptions made in the calculation of the debris flight wind speed, based on industry data for hay bales (Banta, 2012), and the resulting wind speed. In addition, it is also assumed that the haybales remained intact during the flight and were not impacted by any trees or structures along its potential trajectory.

The calculation suggests that at minimum, a debris flight wind speed of about 260 km/h was required to displace the hay bales, a value that is at the high end of the EF3 wind speed range. The maximum values reach well into the EF5 range. This model only provides a simple threshold speed for flight; future work is needed to analyze the potential debris

Table 4
Assumed details on the vehicles used to solve for the debris threshold wind speed.

Van Length [m]	Van Width [m]	Van Height [m]	Van Mass [kg]	ρ_m [kg/m³]	S_p	C_D	C_L	$X_{Threshold}$ [km/h]	$\hat{U}$ [km/h]	Lofting wind speed Haan et al. (2017) [km/h]
5.11	1.92	1.74	1900	110	0.38	0.36	0.351–0.474	287–361	281–352	270

Table 5
Assumed details on the hay bales used to solve for the debris threshold wind speed.

Bale Width [m]	Bale Diameter [m]	Bale Weight [kg]	ρ_m [kg/m³]	S_p	C_D	C_L	$X_{Threshold}$ [km/h]	$\hat{U}$ [km/h]
1.22	1.22	256	180	0.45	0.71–0.83	0.34–0.46	263–364	256–355

flight trajectories. Of particular importance would be to consider the distance that the debris traveled (in this case, several hundred meters at maximum heights of tens of meters) together with an appropriate tornado wind field model, such as those of Twisdale et al. (1981) or Baker and Sterling (2017).

4. Wind speed estimation based on treefall observations

Tree damage and fall patterns are often used to estimate the intensity of tornadoes (Karstens et al., 2013; Lombardo et al., 2015; Godfrey and Peterson, 2017; Rhee and Lombardo, 2018). Tree damage inflicted by a tornado creates a distinctive fall pattern (i.e., converging pattern) due to the flow characteristics of the tornado wind field. Thus, distinct flow parameters and wind speed of the tornado can be estimated by analyzing the fall pattern of trees (treefall analysis). Herein, the treefall analysis introduced in Lombardo et al. (2015) and Rhee and Lombardo (2018) is used to estimate the wind speeds of the Alonsa tornado. In the treefall analysis, a tornado is numerically simulated using a Rankine vortex (RV) and an associated tree fall pattern is generated by enforcing a critical wind speed of treefall (V_c). It is assumed that a treefall will occur when the wind speed exceeds this value. Simulated treefall patterns are then compared to the observed patterns in the Alonsa tornado and iterated until the best matching pattern is found. The parameters used to generate the best match are then used to reconstruct the near-surface wind field of the tornado. The reader is referred to Lombardo et al. (2015) and Rhee and Lombardo (2018) for a discussion of the detailed process.

This tornado wind speed estimation method is particularly useful in forested regions where trees are abundant and structures are sparse. In general, the observed treefall patterns are obtained by "tagging" trees on a geographic information system (GIS); however, tagging a vast number of trees in heavily wooded regions can be time-consuming and labor-intensive. To reduce time and manual labour, a method that automatically detects the treefall pattern of a tornado using image processing tools is presented in Rhee et al. (2021).

In this section, the treefall pattern of the Alonsa tornado acquired by Rhee et al. (2021) is used to estimate the near-surface wind field, independent of the structural damage assessment and debris flight analysis. Unlike Lombardo et al. (2015) and Rhee and Lombardo (2018) where the critical wind speed of treefall parameter was treated as a random variable, the average V_c of the Alonsa tornado is estimated using a mechanistic tree risk model and resistance regression model and the necessary input parameters for V_c are extracted from the aerial imagery using image processing tools. The estimated average V_c is then used as one of the input parameters for treefall analysis.

4.1. Extraction of tree dimensions from aerial imagery

Tree dimensions are necessary parameters for estimating the wind-induced force and resistance of a tree. However, obtaining dimensions

of damaged trees (e.g., projected area) can be often challenging from a ground-based damage survey. Using photogrammetry and similar image processing techniques described in Rhee et al. (2021), not only the treefall pattern can be acquired, but the tree dimensions necessary for calculating V_c can also be extracted remotely. An example demonstrating the extraction process using a sample tree from the Alonsa tornado aerial imagery is provided in Fig. 13. In Fig. 13(a), the sample image is first cropped from the aerial imagery. An RGB color filter that filters specific colors from an image is then applied to extract pixels associated with the damaged tree as shown in Fig. 13(b), followed by a noise filter that removes "small objects" in Fig. 13(c). Although the noise filter removes the background noise, large noise (non-tree) objects that have similar color to trees (e.g., roads, hay bales) are still present. Using an object detection algorithm, the binary image is separated into different objects such that only the pixels belonging to the tree can be selected as shown in Fig. 13(d). For detailed procedure and algorithm for extracting tree-pixels should be referred to Rhee et al. (2021). Finally, the crown and stem of the tree are differentiated manually and the number of pixels is counted for all desired dimensions as shown in Fig. 13(e). With the aerial imagery resolution being 5 cm, the tree dimensions (diameter at breast height, DBH; overall height, h; height of the crown, h_{crw}; stem area A_{stem}; area of the crown, A_{crw}) can be scaled into actual heights and areas, with results provided in Table 6. The geometric dimensions of trees estimated from aerial imagery show comparable results to direct measurements from Peltola et al. (1997). Note that the tree dimensions extracted using image processing are dependent on the number of pixels and thus highly sensitive to the digital number (DN) range used in the RGB filter.

4.2. Critical wind speed of treefall

Once the dimensions are obtained from the aerial imagery, the critical wind speeds for treefall in the Alonsa tornado can be determined by coupling tree critical overturning moment regression models and the HWIND model, a tree wind-resistance model developed by Peltola and Kellomaki (1993) and Peltola et al. (1999). It is assumed that tree failure occurs when the wind-induced force is greater than the resistance of the tree. In the HWIND model, the forces exerted on a tree are typically divided into a horizontally acting wind-induced force and a vertically acting gravitational force. However, the gravitational force is ignored due to the low sensitivity of weight and difficulty of estimating the tree mass from aerial imagery. It was found that 20% change in crown/stem mass resulted in only 1–2% change in V_c (Peltola et al., 1999).

The total wind-induced force (F) and the overturning moment (T) exerted on a tree at height, z, are expressed as

$$F(z) = \frac{1}{2}\rho_a \hat{U}(z)^2 A(z) C_d \quad (11)$$
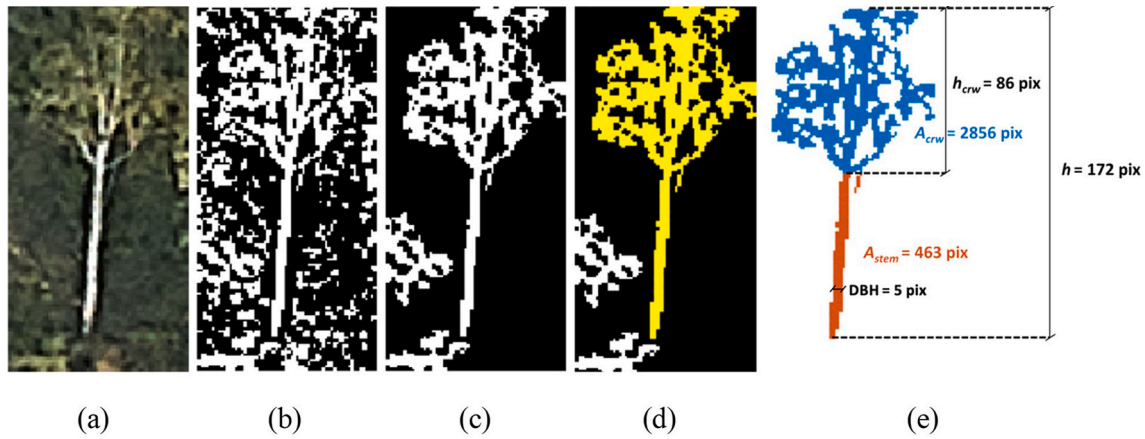
$$T(z) = F(z) \bullet z \quad (12)$$

Fig. 13. Tree dimension extraction process from an aerial photograph; (a) sample tree image cropped from satellite imagery, (b) pixels extracted by RGB color filter, (c) filtered image with "small objects" removed, (d) highlighted pixels deemed to belong to the tree by the object detection algorithm, (e) dimensioned image differentiating between tree crown and stem.

Table 6
Estimation of geometric properties of tree from aerial imagery.

Parameter	DBH	dh	h_{crw}	A_{stem}	A_{crw}
Number of pixels	5	172	86	463	2856
Resolution Scale	5 cm	5 cm	5 cm	25 cm^2	25 cm^2
Actual Dimension	25 cm	8.6 m	4.3 m	1.16 m^2	7.14 m^2

where C_d is the drag coefficient and $\widehat{U}$ is the 3-sec wind gust. Ground-based observations show that most of the trees in the Alonsa region were Trembling Aspen, Balsam Poplar, and other hardwood species (Mansour et al., 2021). A drag coefficient of 0.28 at 20 m/s was measured for Trembling Aspen by Vollsinger et al. (2005). Although the drag coefficient decreases non-linearly with wind speed due to the change in crown shape and the reduction of frontal area (Vollsinger et al., 2005; Enuş et al., 2020) and tree failures are most likely to occur at higher wind speeds, the highest wind speed of drag coefficient available in the literature for Trembling Aspen was 20 m/s. The rate of decreasing of drag coefficient decreases as wind speed increases because the rate of frontal area reduction decreases, indicating that the uncertainty in the drag coefficient will be reduced for higher wind speeds. Sensitivity analysis also showed the effect of drag coefficient on the critical wind speed was not significant. Thus, a constant drag coefficient of 0.28 was assumed for all trees in this study.

The wind speed at height, z, is obtained using the Power Law with a 3-sec gust exponent $\alpha = 1/7$ for Exposure B (American Society of Civil Engineers, 2016). A tree typically fails in two failure modes: (1) stem breakage or (2) uprooting, which occurs when the maximum rupture strength or the root-plate soil plate is exceeded, respectively. However, due to the difficulty of acquiring the soil condition, root mass, and the rupture strength of the trees from aerial imagery, linear regression models of the critical overturning moment of trees, measured from experimental winching tests (Cucchi et al., 2004; Cannon et al., 2015), are used instead to estimate the resistance of the tree (Fig. 14).

A total of 41 trees are sampled, 4 of which are found to have failed by uprooting and the rest by stem breakage. It is important to note that a complete-random sampling is not feasible; only isolated trees are selected due to the difficulty of identifying a single tree among many overlapping fallen trees. This may affect V_c estimation as isolated trees are known to have stronger root systems and larger surface areas (Cucchi et al., 2004). Fig. 15 shows the distribution of estimated V_c of the 41 sample trees plotted against the DBH. The distribution shows an increasing trend as the DBH gets larger with a mean value of 47.5 m/s and a standard deviation of 12.5 m/s. The maximum V_c is estimated at
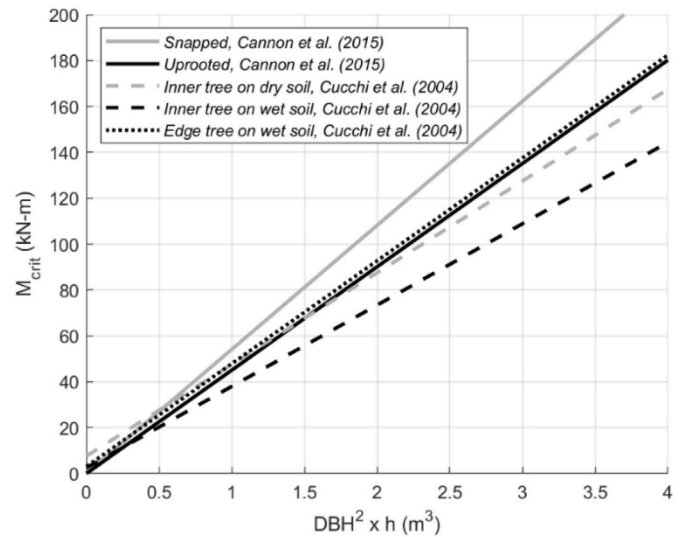

Fig. 14. Regression lines of the critical overturning moment of trees under various conditions.
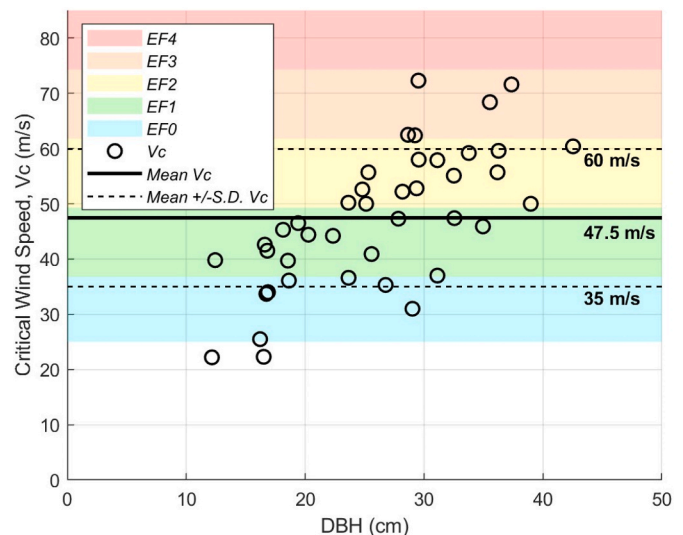

Fig. 15. Critical wind speeds from the treefall analysis for the Alonsa tornado.

73 m/s. This verifies that, based on the condition of the trees observed in the Alonsa tornado path, the tree damage observed there warrants a rating at least as high as EF3. The average V_c result from the Alonsa tornado is higher than those obtained from the Joplin, Missouri (40 m/s) and Naplate, Illinois (34 m/s) tornadoes using a different method (Lombardo et al., 2015; Rhee and Lombardo, 2018). A higher V_c is perhaps expected for the Alonsa tornado because most trees in the region (Trembling Aspen and Balsam Poplar) were tall and slender trees with smaller projected frontal areas (Wang et al., 1998), and they failed by stem breakage, which generally requires greater overturning moment than failure by uprooting (Cannon et al., 2015).

4.3. Wind field estimation

In this section, the final wind speed and other associated parameters of the Alonsa tornado are estimated using the treefall analysis method described in Rhee and Lombardo (2018) and the V_c estimated in section 5.2; a series of treefall patterns are simulated using the RV model with different parameters (a tree fall is simulated when the wind speed exceeds the estimated V_c) until the "best-matching" treefall pattern is found. The observed treefall pattern of the Alonsa tornado is obtained from Rhee et al. (2021). The majority of the treefall pattern showed a converging pattern similar to the general treefall pattern in Rhee and Lombardo (2018) but diverging treefall patterns were also observed on the outskirts of the damage path, which may have been attributed to downburst winds or rear-flank downdraft surge (Fujita, 1981; Karstens et al., 2013). Although the image processing method can rapidly detect tree damage and acquire the treefall pattern, the method cannot distinguish tornadic damage from other non-tornadic damage. Because the main interest of this paper lies in the wind speed estimation of a tornadic event, tornado-induced treefalls are subjectively identified, and only tornadic tree damage is used in the treefall analysis. Sills et al. (2020) provide guidelines for determining non-tornadic damage in a forested area using remote sensing imagery.

Once the tornado-induced tree damage is identified, the tornado intensity can be estimated by analyzing the pattern. The preliminary results of Rhee et al. (2021) suggested an increase in RV parameters over time, based on the change in treefall directions along the track. The parameters that significantly dictate the treefall pattern are G_{max} and α_T, which are the ratio between the rotational wind speed and the translational speed of the tornado (V_T) and the angle between the rotational and radial velocity, respectively (Rhee and Lombardo, 2018). An increase in these two parameters indicates a growth of tornado intensity and rotation (tangential wind speed component) over time. Additionally, a significant increase in the damage width (DW) along the entire

track suggests a possible increase in the radius of maximum wind (*RMW*).

In order to assess the wind field and visualize the evolution of the tornado, multiple transects of treefall patterns that show significantly different treefall directions and DW are selected to perform treefall analysis. Considerable changes in the treefall pattern along the tornado path are indicative of changes in tornado structure/intensity. A total of six transects are selected and the treefall directions within the six transects are averaged in 50 m × 200 m bins, showing the prevailing wind direction in each bin.

Fig. 16 shows the observed treefall patterns along the six transects, normalized in the translation direction. Transect #1 displays a forward falling treefall pattern (low G_{max}) that suggests a relatively weaker tornado and transects #4–6 show a backward falling pattern near the center of the tornado (high G_{max}) that suggests a relatively stronger tornado (Rhee et al., 2021). Transects #2 and 3 exhibit a transition pattern with a mixture of forward and backward falling treefall patterns. Forward and backward falling patterns are defined as trees falling in the direction of tornado translation and trees falling against the tornado translation, respectively. Herein, the tornado moved northeast along the estimated centerline shown in Fig. 16. Tornadoes with backward falling patterns indicate a strong rotation and inflow, causing trees to fall towards the center of the vortex, which is typically found in relatively stronger tornadoes (e.g., EF3 or higher) (Lombardo et al., 2015; Rhee and Lombardo, 2018).

Using the estimated average value of V_c, tornado-induced treefall patterns with over three million different parameter combinations are simulated for each transect and compared to the observed patterns for independent parameter estimations. For the first set of iterations, the V_T is treated as a random variable within a range of 12–20 m/s and converged to a value of 17 m/s. Notably, the 17 m/s V_T estimation complements the mean storm motion vector that was estimated at 18 m/s by the College of DuPage NeXt Generation Weather Lab (College of DuPage, 2018). The second set of iterations is made using a constant V_T. The estimated RV parameters and the maximum wind speed, $\widehat{U}_{max}$, for each transect using a fixed V_T (17 m/s) and V_c (47.5 m/s) are summarized in Table 7. The total maximum wind speed (88 m/s) occurred at transects #4 and 6, corresponding to a low-end EF5 wind speed. Fig. 17 shows the change in RV parameters along the path. A general increasing trend in all parameters suggests a steady growth of tornado intensification and size as the tornado traversed over the forest. On the other hand, α_T is increased until the tornado reached its strongest rotation at transect #4 and then decreased after transect #4, indicating a reduction in the rotation but still maintaining inflow into the tornado given that
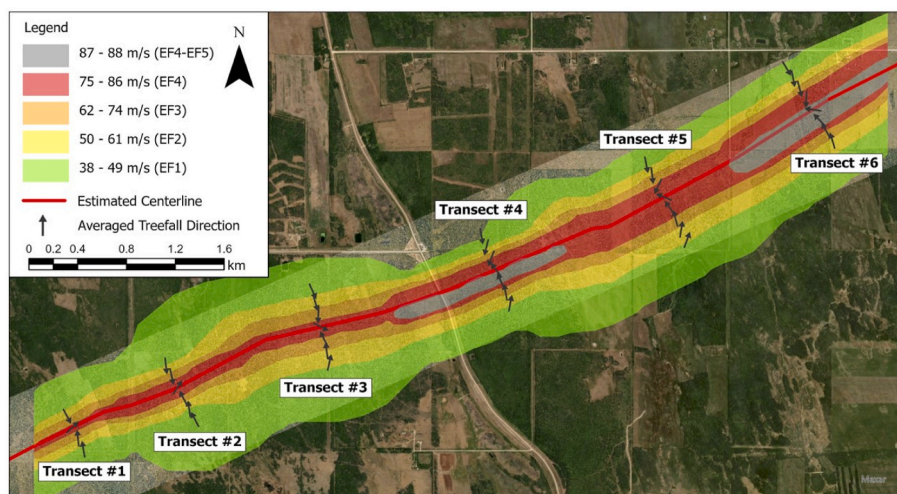

Fig. 16. Observed treefall patterns at six transects along the Alonsa tornado damage path, overlaying contours showing the estimated near-surface wind speeds.

Table 7
Best-matched RV parameters and the maximum wind speed in the Alonsa tornado at each transect, with constant VT (17 m/s) and VC (45.7 m/s).

Transect #	G_{max}	α_T (°)	RMW (m)	φ[a]	$\widehat{U}_{max}$ [m/s (km/h)]
1	3.5	5	90	0.5	76 (274)
2	3.7	0	110	0.6	80 (288)
3	3.5	10	150	0.5	76 (274)
4	4.2	33	140	0.8	88 (317)
5	4.0	23	180	0.7	85 (306)
6	4.2	20	190	0.8	88 (317)

[a] Decay exponent in the RV model.

the $\widehat{U}_{max}$ is at its maximum. Overall, the best-matched RV parameters match the expectations from the preliminary result from Rhee et al. (2021). Using the estimated parameters at each location, the near-surface wind field of the Alonsa tornado is recreated as shown in Fig. 16. Unfortunately, the damaged area near the end of the track (Sites 7 and 8) did not have enough trees (see Fig. 9) to perform the treefall analysis.

5. Comparison of wind speed estimation across analysis methods

The conventional EF-Scale damage survey method for wind speed estimation has several known limitations. The assessment of structural damage depends on whether a building was directly hit and the quality of construction. Tree DIs allow a wind speed assessment up to only EF3. In a worst-case scenario, an intense tornado can strike an area with no DIs and receive only a default EF0 rating (wind speed assumed to be at least 90 km/h, the lower bound of EF0 range for the Canadian EF Scale).

The treefall analysis method can avoid these limitations, as long as tree density is high enough for the method to be applied. Similarly, the debris flight approach can estimate wind speeds across the full EF-scale spectrum, as long as relatively simple objects and their approximate flight paths can be identified (Environment Canada, 2013). comparison of the treefall analysis results to nearby EF-Scale method wind speed estimates is shown in Fig. 18, and further summarized in Table 8. The treefall and debris flight wind speed estimates are consistently higher than that from the conventional EF-Scale assessment. The maximum wind speed estimated from the structural investigation is 275 km/h at Site 3, where there was a direct hit, but construction was sub-standard. In nearby regions where tree density was sufficient, the treefall analysis estimates approximately 306 km/h, with the maximum wind speed of 317 km/h occurring at Site 2, and then again after the tornado passed Site 3. Further along the path, the debris flight assessment using simple hay bales estimates wind speeds of 256–355 km/h between Site 4/5 and Site 6, while damage to nearby structures suggests a range of 230–245 km/h. Overall, both research methods resulted in higher maximum wind speed estimates than using the conventional EF-Scale method.
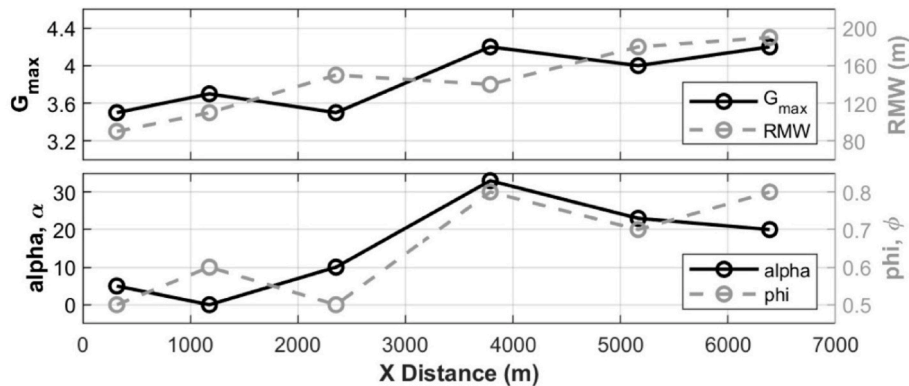

Fig. 17. Change in best-matched parameters along the damage track of the Alonsa tornado. Each plotted circle represents the location of a transect.
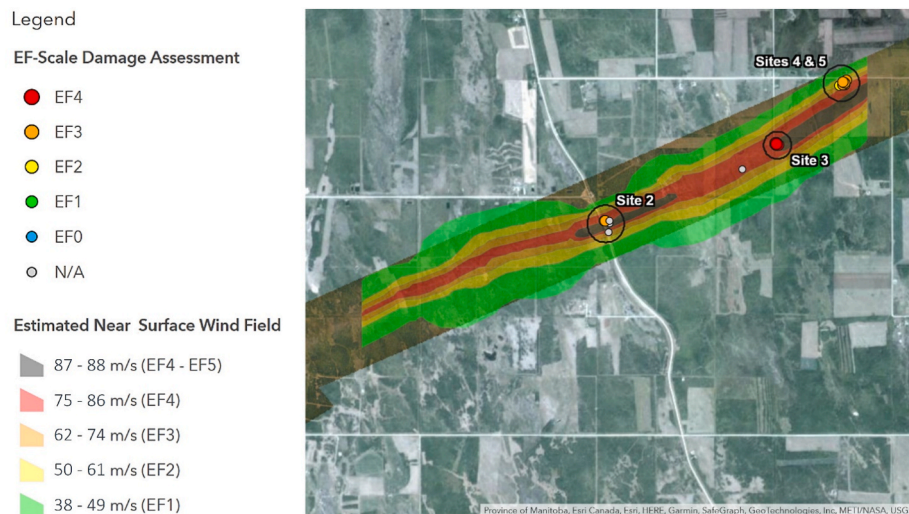

Fig. 18. Map of Alonsa tornado wind field showing wind speed contours from treefall analysis and damage site estimates based on the conventional EF-Scale damage survey method.

Table 8
Comparison of wind speed estimation methods in vicinity of each ground survey site. Treefall pattern estimates are taken as a mean of nearest transects if no transect is in the immediate vicinity of the site; nearest transects are noted in parentheses. All speeds reported in km/h.

Site	Structural EF-Scale assessment (greater of FR12/SBO)	C-T EF-Scale assessment	Debris threshold flight wind speed	Treefall pattern analysis (transect)
0	–	150	–	–
1	–	235	–	274 (1)
2	230	–	–	296 (3/4 avg)
3	275	235	–	306 (5)
4	180	–	256-355 (Hay bales)	317 (6)
5	245	–	256-355 (Hay bales)	–
6	230	–	256-355 (Hay bales)	–

6. Conclusions

Research methods for wind speed estimation using ground and aerial survey data collected by the Northern Tornadoes Project were applied to the EF4-rated tornado in Alonsa, Manitoba, Canada, that occurred on August 3, 2018. This allowed comparison between the maximum wind speed and EF-Scale rating assigned using typical EF-Scale assessment. There is good agreement between the two research methods, with both estimating higher wind speeds than those obtained from the conventional EF-Scale assessment (using DIs with the Canadian EF Scale).

The EF-Scale assessment estimated a maximum, 3-s gust wind speed of 275 km/h, corresponding to a low-end EF4 rating. It should be noted that an EF-Scale assessment of EF5 was not possible due to the substandard construction of the residences that experienced the highest tornado wind speeds. The treefall pattern assessments estimated higher maximum wind speed of 317 km/h. This wind speed corresponds to low-end EF5, which may more accurately represent the maximum wind speeds along the path of the Alonsa tornado.

Although the debris flight analysis is able to provide an estimate of the threshold wind velocity for lofting, there are many simplifying assumptions that should be addressed in future work. There is a large degree of uncertainty since the analysis does not take into account the overall complexity of a tornadic wind field. Accounting for the debris trajectory in the tornado-vortex wind field should be done to more completely model debris flight, rather than just the onset failure wind speed. A greater variety of object types should also be considered. The treefall analysis, by utilizing the patterns of failure and tornado vortex characteristics, is able to capture the wind field along the path of a tornado to a significant extent. Yet there are still uncertainties related to various, necessary assumptions. These non-conventional wind speed estimation methods have been shown to be useful in the analysis of a violent tornado event – providing inter-method consistency and a potential increase in accuracy. However, further research is required to ensure that they can be used as part of operational assessments of tornado intensity.

Credit author statement

Sarah A. Stevenson: Methodology, Formal Analysis, Investigation, Data Curation, Writing – Original Draft, Visualization. **Connell S. Miller:** Methodology, Formal Analysis, Investigation, Data Curation, Writing – Original Draft, Visualization. **David M.L. Sills:** Writing – Review & Editing, Supervision, Resources, Project Administration, Funding Acquisition. **Gregory A. Kopp:** Conceptualization, Validation, Writing – Review & Editing, Supervision, Resources, Project Administration, Funding acquisition. **Daniel M. Rhee:** Methodology, Formal Analysis, Data Curation, Writing – Original Draft, Visualization,

Software. **Franklin T. Lombardo:** Conceptualization, Validation, Writing – Review & Editing, Supervision, Software.

Data availability

Data will be made available on request.

List of Symbols

A	Reference area
A_{crw}	Crown area
A_{stem}	Stem area
C_D	Drag coefficient
C_L	Lift coefficient
DBH	Diameter of tree at breast height
DW	Damage width
F	Wind-induced force
g	Gravitational constant
G_{max}	Ratio between the rotational wind speed and translational speed of a tornado
h	Overall tree height
h_{crw}	Height of crown
l	Characteristic dimension of debris object
M_{crit}	Critical overturning moment
NDVI	Normalized Difference Vegetation Index
$NDVI_{After}$	NDVI calculated from imagery taken following the event
$NDVI_{Before}$	NDVI calculated from imagery taken prior to the event
$NDVI_{(\%Change)}$	Percent change in NDVI from comparison of two images
NIR	Reflection in near-infrared spectrum
RED	Reflection in red spectrum
RMW	Radius of maximum wind
S_p	Shape factor for debris object
T	Overturning moment
U	Wind speed
$\hat{U}$	3-s peak gust speed
U_m	Speed of object
$\hat{U}max$	Maximum wind speed estimate
Vc	Threshold wind speed for tree fall
V_{Cuboid}	Volume of representative cuboid
V_{Debris}	Volume of debris object
$V_{Ellipsoid}$	Volume of representative ellipsoid
V_T	Translational speed of tornado
$v_{Threshold}$	Threshold wind speed for lofting of object
X	Horizontal component of wind speed
x_m	Horizontal component of object speed
Z	Vertical component of wind speed
z	Height above ground

z_m	Vertical component of object speed
α	3-s gust exponent
α_T	Angle between rotational and radial velocity components
Θ	Angle between resultant wind speed and horizontal axis
ρ_a	Air density
ρ_m	Density of debris object
ϕ	Decay exponent in Rankine Vortex model

References

American Society of Civil Engineers, 2016. Minimum Design Loads for Buildings and Other Structures. Structural Engineering Institute, Reston, VA.

Amini, M.O., van de Lindt, J.W., 2014. Quantitative insight into rational tornado design wind speeds for residential wood-frame structures using fragility approach. J. Struct. Eng. 140 (7) https://doi.org/10.1061/(ASCE)ST.1943-541X.0000914.

Baker, C.J., 2007. The debris flight equations. J. Wind Eng. Ind. Aerod. 95 (5), 329–353. https://doi.org/10.1016/j.jweia.2006.08.001.

Baker, C.J., Sterling, M., 2017. Modelling wind fields and debris flight in tornadoes. J. Wind Eng. Ind. Aerod. 168, 312–321. https://doi.org/10.1016/j.jweia.2017.06.017.

Banta, J., 2012. Bale weight: how important is it? Agrilife Extension E319, 1–12.

Bech, J., et al., 2009. Tornado damage analysis of a forest area using site survey observations, radar data, and a simple analytical vortex model. Atmos. Res. 93 (1), 118–130. https://doi.org/10.1016/j.atmosres.2008.10.016.

Beck, V., Dotzek, N., 2010. Reconstruction of near-surface tornado wind fields from forest damage. J. Appl. Meteorol. Climatol. 49 (7), 1517–1537. https://doi.org/10.1175/2010JAMC2254.1.

Cannon, J.B., Barrett, M.E., Peterson, C.J., 2015. The effect of species, size, failure mode, and fire-scarring on tree stability. For. Ecol. Manag. 356 (15), 196–203. https://doi.org/10.1016/j.foreco.2015.07.014.

Chai, V., et al., 2019. A model for aerodynamic coefficients of rock-like debris. Compt. Rendus Mec. 347 (1), 19–32. https://doi.org/10.1016/j.crme.2018.10.001.

Chen, G., Lombardo, F.T., 2019. An analytical pattern-based method for estimation of a near-surface tornadic wind field. J. Wind Eng. Ind. Aerod. 194 https://doi.org/10.1016/j.jweia.2019.103999.

College of DuPage, 2018. Canadian upper air soundings. https://weather.cod.edu/analysis/. (Accessed 17 February 2022).

Cucchi, V., et al., 2004. Root anchorage of inner and edge trees in stands of Maritime pine (Pinus pinaster Ait.) growing in different podzolic soil conditions, 460-266 Trees (Berl.) 18. https://doi.org/10.1007/s00468-004-0330-2.

Durst, C.S., 1960. Wind speeds over short periods of time. Meteorological Magazine 89, 181–186.

Edwards, R., et al., 2013. Tornado intensity estimation: past, present, and future. Bull. Am. Meteorol. Soc. 94, 641–653. https://doi.org/10.1175/BAMS-D-11-00006.1.

Ellingwood, B.R., Rosowsky, D.V., Li, Y., Kim, J.H., 2004. Fragility assessment of light-frame wood construction subjected to wind and earthquake hazards. J. Struct. Eng. 130 (2), 1921–1930. https://doi.org/10.1061/(ASCE)0733-9445(2004)130:12(1921).

Enuş, M., Dellwik, E., Mann, J., Hangan, H., Costache, A., 2020. Three-dimensional measurements of tree crown movement using an infrared time-of-fight camera. Exp. Fluid 61, 1–13. https://doi.org/10.1007/s00348-020-03053-y.

Environment Canada, 2013a. Environment and climate change Canada: enhanced Fujita scale. https://ec.gc.ca/meteo-weather/default.asp?lang=En&n=41E875DA-1 [Accessed June 2022].

Frelich, L.E., Ostuno, E.J., 2012. Estimating wind speeds of convective storms from tree damage. Elect. J. Severe Storms Meteor. 7 (9), 1–19.

Fujita, T.T., 1971. Proposed Characterization of Tornados and Hurricanes by Area and Intensity. Satellite and Mesometeorology Research Project Report 91. University of Chicago, Chicago, IL.

Fujita, T.T., 1981. Tornadoes and downbursts in the context of generalized planetary scales. J. Atmos. Sci. 38 (8), 1511–1534. https://doi.org/10.1175/1520-0469(1981)038<1511:TADITC>2.0.CO;2.

Gardiner, B.H., Peltola, B.H., Kellomaki, S., 2000. Comparison of two models for predicting the critical wind speeds required to damage coniferous trees. Ecol. Model. 129, 1–23. https://doi.org/10.1016/S0304-3800(00)00220-9.

Godfrey, C.M., Peterson, C.J., 2017. Estimating Enhanced Fujita scale levels based on forest damage severity. Weather Forecast. 32 (1), 243–252. https://doi.org/10.1175/WAF-D-16-0104.1.

Haan, F.L., Sarkar, P.P., Kopp, G.A., Stedman, D.A., 2017. Critical wind speeds for tornado-induced vehicle movements. J. Wind Eng. Ind. Aerod. 160, 1–8. https://doi.org/10.1016/j.jweia.2017.04.014.

Haines, M., Taylor, I., 2018. Numerical investigation of the flow field around low rise buildings due to a downburst event using large Eddy Simulation. J. Wind Eng. Ind. Aerod. 172, 12–30. https://doi.org/10.1016/j.jweia.2017.10.028.

Holmes, J.D., 2004. Trajectories of spheres in strong winds with application to wind-borne debris. J. Wind Eng. Ind. Aerod. 92 (1), 9–22. https://doi.org/10.1016/j.jweia.2003.09.031.

Huo, S., Hemida, H., Sterling, M., 2020. Numerical study of debris flight in a tornado-like vortex. J. Fluid Struct. 99 https://doi.org/10.1016/j.jfluidstructs.2020.103134.

Jesson, M., Sterling, M., Letchford, C., Haines, M., 2015. Aerodynamic forces on generic buildings subject to transient, downburst-type winds. J. Wind Eng. Ind. Aerod. 137, 58–68. https://doi.org/10.1016/j.jweia.2014.12.003.

Karstens, C.D., Gallus, W.A., Lee, B.D., Finley, C.A., 2013. Analysis of tornado-induced tree fall using aerial photography from the Joplin, Missouri, and Tuscaloosa-Birmingham, Alabama, Tornadoes of 2011. J. Appl. Meteorol. Climatol. 52 (2), 1049–1068. https://doi.org/10.1175/JAMC-D-12-0206.1.

Kingfield, D., deBeurs, K., 2017. Landsat identification of tornado damage by land cover and an evaluation of damage recovery in forests. J. Appl. Meteorol. Climatol. 56 (4), 965–987. https://doi.org/10.1175/JAMC-D-16-0228.1.

Kopp, G.A., et al., 2016. Assessment of wind speeds based on damage observations from the Angus (Ontario) Tornado of 17 June 2014. Can. J. Civ. Eng. 44 (1), 37–47. https://doi.org/10.1139/cjce-2016-0232.

Kopp, G.A., Morrison, M.J., Kordi, B., Miller, C., 2011. A method to assess peak storm wind speeds using detailed damage surveys. Eng. Struct. 33 (1), 90–98. https://doi.org/10.1016/j.engstruct.2010.09.021.

Kordi, B., Kopp, G.A., 2011. Effects of initial conditions on the flight of windborne plate debris. J. Wind Eng. Ind. Aerod. 99 (5), 601–614. https://doi.org/10.1016/j.jweia.2011.02.009.

Lee, K.H., Rosowsky, D.V., 2005. Fragility assesment for roof sheathing failure in high wind regions. Eng. Struct. 27 (6), 857–868. https://doi.org/10.1016/j.engstruct.2004.12.017.

Lombardo, F.T., Roueche, D.B., Prevatt, D.O., 2015. Comparison of two methods of near-surface wind speed estimations in the 22 May, 2011 Joplin, Missouri Tornado. J. Wind Eng. Ind. Aerod. 138, 87–97. https://doi.org/10.1016/j.jweia.2014.12.007.

Magsig, M., Dickens-Micozzi, M., Yuan, M., 2000. Analysis of Tornado Damage on May 3rd 1999 Using Remote Sensing and GIS Methods on High-Resolution Satellite Imagery. American Meteorological Association, Orlando, FL, pp. 9–12.

Mansour, M.A., et al., 2021. Estimating wind damage in forested areas due to tornadoes. Forests 12 (1). https://doi.org/10.3390/f12010017.

McCarthy, P.J., Carlsen, D., Slipec, J., 2008. *Elie, Manitoba, Canada, June 22, 2007: Canada's First F5 Tornado.* s.L. American Meteorological Society.

McDonald, J.R., Mehta, K.C., Smith, D.S., Womble, J.A., 2009. The Enhanced Fujita Scale: Development and Implementation. American Society of Civil Engineers, Washington, D.C. https://doi.org/10.1061/41082(362)73.

Mehta, K.C., 2013. Development of EF-scale for tornado intensity. J. Disaster Res. 8 (6) https://doi.org/10.20965/jdr.2013.p1034.

Molthan, A.L., Bell, J.R., Cole, T.A., Burks, J.E., 2014. Satellite-based identification of tornado damage tracks from the 27 April 2011 severe weather outbreak. J. Operat. Meteor. 2 (16), 191–208. https://doi.org/10.15191/nwajom.2014.0216.

Morrison, M.J., et al., 2014. Assessment of damage to residential construction from the tornadoes in Vaughan, Ontario, on August 2009. Can. J. Civ. Eng. 41, 550–558. https://doi.org/10.1139/cjce-2013-0570.

Myint, S.W., Yuan, M., Cerveny, R., Giri, C.P., 2008. Comparison of remote sensing image processing techniques to identify tornado damage areas from Landsat TM data. Sensors 8 (2), 1128–1156. https://doi.org/10.3390/s8021128.

National Oceanic and Atmospheric Administration, 2020. Storm prediction center mesoscale analysis. https://www.spc.noaa.gov/exper/mesoanalysis/. (Accessed 3 June 2022).

Northern Tornadoes Project, 2020. Open data for the northern tornadoes Project. https://ntpopendata-westernu.opendata.arcgis.com/. (Accessed 20 November 2021).

Peltola, H., Kellomaki, S., 1993. A mechanistic model for calculating windthrow and stem breakage of Scots pines at stand age. Silva Fenn. 27 (2) https://doi.org/10.14214/sf.a15665.

Peltola, H., Kellomaki, S., Visnen, H., Ikonen, V.-P., 1999. A mechanistic model for assessing the risk of wind and snow damage to single trees and stands of Scots pine, Norway spruce, and birch. Can. J. For. Res. 29 (6), 647–661. https://doi.org/10.1139/x99-029.

Peltola, H., Nykänen, M.-L., Kellomäki, S., 1997. Model computations on the critical combination of snow loading and windspeed for snow damage of Scots pine, Norway spruce and birch sp. at stand edge. For. Ecol. Manag. 95 (1), 229–241. https://doi.org/10.1016/S0378-1127(97)00037-6.

Peterson, R.E., 1992. Johannes Letzmann: a pioneer in the study of tornadoes. Weather Forecast. vol. 7, 166–184. https://doi.org/10.1175/1520-0434(1992)007<0166:JLAPIT>2.0.CO;2.

Radhika, S., Tamura, Y., Matsui, M., 2012. Use of post-storm images for automated tornado-borne debris path identification using texture-wavelet analysis. J. Wind Eng. Ind. Aerod. 107, 202–213. https://doi.org/10.1016/j.jweia.2012.04.016.

Radhika, S., Tamura, Y., Matsui, M., 2015. Cyclone damage detection on building structures from pre-and post-satellite images using wavelet based pattern recognition. J. Wind Eng. Ind. Aerod. 136, 23–33. https://doi.org/10.1016/j.jweia.2014.10.018.

Rhee, D.M., Lombardo, F.T., 2018. Improved near-surface wind speed characterization using damage patterns. J. Wind Eng. Ind. Aerod. 180, 288–297. https://doi.org/10.1016/j.jweia.2018.07.017.

Rhee, D.M., Lombardo, F.T., Kadowaki, J., 2021. Semi-automated tree-fall pattern identification using image processing technique: application to Alonsa, MB tornado. J. Wind Eng. Ind. Aerod. 208, 1–11. https://doi.org/10.1016/j.jweia.2020.104399.

Rosowsky, D.V., Ellingwood, B.R., 2002. Performance-based engineering of wood-frame housing: fragility analysis methodology. J. Struct. Eng. 128 (1), 32–38. https://doi.org/10.1061/(ASCE)0733-9445(2002)128:1(32).

Roueche, D.B., Lombardo, F.T., Prevatt, D.O., 2017. Empirical approach to evaluating the tornado fragility of residential structures. J. Struct. Eng. 143 (9) https://doi.org/10.1061/(ASCE)ST.1943-541X.0001854.

Roueche, D.B., Prevatt, D.O., 2013. Residential damage patterns following the 2011 Tuscaloosa, AL and Joplin, MO tornadoes. J. Disaster Res. 8 (6), 1061–1067. https://doi.org/10.20965/jdr.2013.p1061.

Sills, D.M., et al., 2020. The Northern Tornadoes Project - Uncovering Canada's True Tornado Climatology. Bulletin of the American Meteorological Society. https://doi.org/10.1175/BAMS-D-20-0012.1.

Sills, D.M.L., McCarthy, P.J., Kopp, G.A., 2014. Implementation and Application of the EF-Scale in Canada. American Meteorological Society, Madison, WI.

Tsutsui, T., 2008. Flow around a sphere in a plane turbulent boundary layer. J. Wind Eng. Ind. Aerod. 96 (6–7), 779–792. https://doi.org/10.1016/j.jweia.2007.06.031.

Twisdale, L.A., Dunn, W.L., Horie, Y., Davis, T.L., 1981. Tornado Missile Simulation and Design Methodology. Model verification and database updates, vol. 2. Report prepared by Research Triangle Institute, Research Triangle Park, North Carolina.

Vollsinger, S., et al., 2005. Wind tunnel measurements of crown streamlining and drag relationships for several hardwood species. Can. J. For. Res. 35 (5), 1238–1249. https://doi.org/10.1139/x05-051.

Wang, Y., Titus, S.J., LeMay, V.M., 1998. Relationships between tree slenderness coefficients and tree or stand characteristics for major species in boreal mixedwood forests. Can. J. For. Res. 28 (8), 1171–1183. https://doi.org/10.1139/x98-092.

Wills, J.A., Lee, B.E., Wyatt, T.A., 2002. A model of wind-borne debris damage. J. Wind Eng. Ind. Aerod. 90, 555–565. https://doi.org/10.1016/S0167-6105(01)00197-0.

Wind Science and Engineering Centre, 2006. A Recommendation for an Enhanced Fujita Scale. Texas Tech University, Lubbock, TX.

Womble, J.A., Mehta, K.C., Adams, B.J., 2007. Automated Building Damage Assessment Using Remote-Sensing Imagery. Long Beach, CA, ASCE.

Womble, J.A., Wood, R.L., Mohammadi, M.E., 2018. Multi-scale remote sensing of tornado effects. frontiers in Built Environment 4 (66). https://doi.org/10.3389/fbuil.2018.00066.

Womble, J.A., et al., 2017. Reality Capture for Tornado Damage to Structures. ASCE, Reston, VA, pp. 134–144.

Yuan, M., Dickens-Micozzi, M., Magsig, M.A., 2002. Analysis of tornado damage tracks from the 3 May tornado outbreak using multispectral satellite imagery. Weather Forecast. 17, 382–398. https://doi.org/10.1175/1520-0434(2002)017<0382:AOTDTF>2.0.CO;2.

Zhao, J., Guirong, Y., Han, D., 2021. A review of approaches to simulate windborne debris dynamics in wind fields. J. Wind Eng. Ind. Aerod. 212 https://doi.org/10.1016/j.jweia.2021.104597.